
OPTIMIZING CARBON STORAGE OPERATIONS FOR LONG-TERM SAFETY

Yizheng Wang
Earth and Planetary Sciences
Stanford University
Stanford, CA 94305
yizhengw@stanford.edu

Markus Zechner
Earth and Planetary Sciences
Stanford University
Stanford, CA 94305
mzechner@stanford.edu

Gege Wen
Energy Science and Engineering
Stanford University
Stanford, CA 94305
gegewen@stanford.edu

Anthony Louis Corso
Aeronautics and Astronautics
Stanford University
Stanford, CA 94305
acorso@stanford.edu

John Michael Mern
Aeronautics and Astronautics
Stanford University
Stanford, CA 94305
jmern91@stanford.edu

Mykel J. Kochenderfer
Aeronautics and Astronautics
Stanford University
Stanford, CA 94305
mykel@stanford.edu

Jef Karel Caers
Earth and Planetary Sciences
Stanford University
Stanford, CA 94305
jcaers@stanford.edu

April 20, 2023

ABSTRACT

To combat global warming and mitigate the risks associated with climate change, carbon capture and storage (CCS) has emerged as a crucial technology. However, safely sequestering CO₂ in geological formations for long-term storage presents several challenges. In this study, we address these issues by modeling the decision-making process for carbon storage operations as a partially observable Markov decision process (POMDP). We solve the POMDP using belief state planning to optimize injector and monitoring well locations, with the goal of maximizing stored CO₂ while maintaining safety. Empirical results in simulation demonstrate that our approach is effective in ensuring safe long-term carbon storage operations. We showcase the flexibility of our approach by introducing three different monitoring strategies and examining their impact on decision quality. Additionally, we introduce a neural network surrogate model for the POMDP decision-making process to handle the complex dynamics of the multi-phase flow. We also investigate the effects of different fidelity levels of the surrogate model on decision qualities.

Main

On our current trajectory, climate models project the global temperature will be 2.8°C hotter at the end of this century [1], which almost doubles the 1.5°C target set by the Paris agreement. Failing to curb greenhouse emissions by transitioning to a low-carbon economy is catastrophic. A report published by the Intergovernmental Panel on Climate Change (IPCC) in 2018 suggests even a half a degree increase in global temperature from 1.5°C to 2°C can have significant negative impacts on human and natural systems [2, 3]. As temperatures continue to rise, the implications and risks associated with climate change become more severe, affecting a wide range of areas from flood to drought, with disastrous consequences on food supply and ecosystems [4, 5, 6].

Many technologies can help to reduce global warming, such as renewable energy sources, technologies to improve efficiency, nuclear, and carbon capture and storage (CCS) [7, 8, 9, 10]. Among these technologies, CCS is the only one that can reduce CO₂ emissions from large centralized sources [11]. Many mitigation portfolios and emission reduction approaches, such as those assessed by IPCC and International Energy Agency (IEA), include CCS [12, 13, 14]. It is essential for addressing climate change and decarbonizing of the global energy system.

CCS is designed to capture CO₂ emissions from large industrial sources, such as power plants and industrial facilities, and then transport and store them underground. The captured CO₂ is typically injected into underground geological formations, such as depleted oil and gas reservoirs, saline aquifers, and coal seams [15, 16]. Saline aquifers have the highest CO₂ storage potential compared to other geological storage options, making them important prospects to scale CCS [17].

By 2022, 20 countries are already developing and operating more than 130 CO₂ storage sites [18]. However, sequestering CO₂ into geological formations for long-term storage comes with many subsurface technological challenges and safety concerns. Although CO₂ sequestration projects may seem similar to other subsurface applications that involve working with the flow in porous media, such as groundwater or oil and gas [19, 20], they pose unique challenges. First, less is known about saline aquifers than oil and gas reservoirs, resulting in significantly higher subsurface uncertainty. Second, one must account for the complex physical and chemical processes such as trapping mechanisms, mineral precipitations, and geomechanics that result from interactions between supercritical CO₂, brine, and rock [21]. Injection of CO₂ into geological formations comes with significant risks, such as induced earthquakes, fractured cap rocks, and reactivation of faults that can lead to CO₂ leakage, harming human life and the environment [22]. Thus, any decisions made in the course of a carbon storage project, such as injector locations, injection rates, and monitoring and mitigation strategies, are safety critical. Overall, the inherent subsurface uncertainty combined with complex physio-chemical processes imposes challenging decision problems for safe and effective carbon storage operations that require tight coupling of information gathering and sequential planning.

The Partial Observable Markov Decision Process (POMDP) is a framework for making sequential decisions under uncertainties (see Methods) [23]. The framework has been successfully applied to many domains, such as autonomous driving, gaming, and healthcare [24, 25, 26, 27]. Optimization of decision strategies within this framework has resulted in systems that perform better than human decision-makers and other state-of-the-art techniques [28].

As shown in Fig 1, optimizing carbon storage operations requires multidisciplinary knowledge, including computer science, geology, engineering, economics, and politics. In a general POMDP formulation for carbon storage, the states may include the geological and engineering characteristics of a subsurface reservoir, flow properties, and joint space of well types, controls, and configurations. The actions may include running well tests, drilling wells, setting well controls, and even abandoning the project. The observations can come from various sources, including local high-resolution observations through boreholes and spatial observations such as seismic signals through active and passive monitoring [29, 30]. The transition function is defined by the complex simulation of flow and transport in porous media that govern the injection and migration of the CO₂ plume. The objective is to maximize the amount of sequestered CO₂ in a subsurface reservoir with some unknown properties and ensure safety for the long term. In carbon storage operations, it is necessary to consider the vast number of scenarios that arise from the high-dimensional state, action, and observation spaces over long planning horizons. This combinatorial problem presents a significant challenge for humans to find the optimal sequence of actions, especially when considering the incorporation of present and future information gathering. We propose an effective way to efficiently search for the best sequence of actions within this complex decision-making space that maximizes expected discounted return.

We formulate the carbon storage problem as a POMDP and solve it using approximate belief state planning. We show the importance of automated decision-making systems for ensuring safe operations by comparing algorithmically generated decisions against human judgments. We demonstrate how reasoning about future information is crucial for safety. In addition, we exemplify how planning over complex dynamics such as multi-phase flow becomes feasible when using a neural network surrogate model.

3D saline aquifer reservoir

To demonstrate the usage of the decision systems in real-world carbon capture operations, we present a 3D saline aquifer reservoir. The aquifer is modeled by a set of engineering parameters and a 3D geological porosity map. We have CO₂ injectors, which inject CO₂ for a fixed period, and monitoring wells, which can be used to observe CO₂ saturation. After the injection period, CO₂ injection ceases. However, the CO₂ still moves and spreads due to the gravitational and buoyancy forces for a more extended time, referred to as the post-injection period. The injected CO₂ can be classified into three categories: exited, free, and trapped. The exited CO₂ indicates the injected CO₂ has leaked

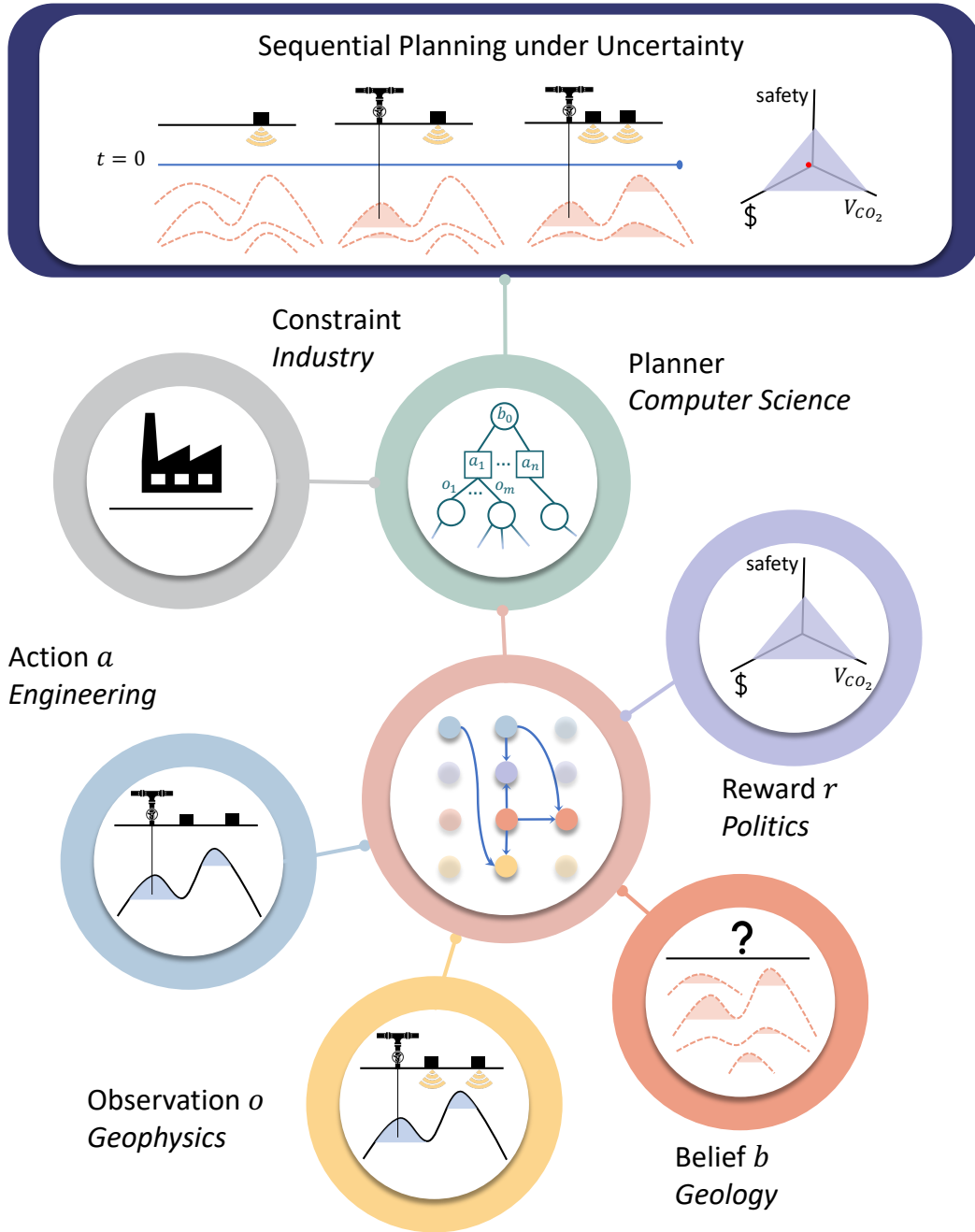


Figure 1: Optimizing for carbon storage operations.

out of the aquifer. The free CO₂ is CO₂ that remains in the aquifer but is not physically bounded and is, therefore, movable. The trapped CO₂ is already in equilibrium and chemically or physically trapped within the aquifer.

The POMDP formulation for the 3D example is shown in Fig. 2a. The state is defined by the joint space of well configurations, the amount of trapped, free, and exited CO₂, and the 3D porosity map. The porosity field remains unknown. The action space is the locations where the wells may be placed, including both CO₂ injectors and monitoring wells. All wells measure the porosity at the well locations. The monitoring wells observe a time history of CO₂ saturation. All observations contain normally distributed noise. The transition dynamics are encoded in a multi-phase flow simulator. It simulates how CO₂ migrates and calculates the mass of each portion of injected CO₂ for the entire injection and post-injection periods. The reward function penalizes the total amount of CO₂ escaping from the aquifer and the free CO₂ and positively rewards the total trapped CO₂ mass, where Δm_{exited} , Δm_{free} , and $\Delta m_{\text{trapped}}$ are, respectively, the changes in exited, free, and trapped CO₂ between states s and s' .

Reducing computational time using a surrogate model

While planning, the belief state planning approach simulates future scenarios and reasons how future information would affect the current decision. This process requires a large number of physical simulations. In our work, this implies our approach needs many simulation episodes of external multi-phase flow in porous media, which is highly computationally intensive (minutes to hours per simulation). To make planning feasible under a multi-phase flow environment, we use a deep learning-based surrogate model as an alternative to numerical simulation. Once trained, the surrogate model provides significant speed-up compared to traditional simulation while maintaining comparable accuracy. Therefore, surrogate models enable efficient repetitive forward simulations needed by our approach.

We use two surrogate models to predict multi-phase flow responses during the injection and post-injection period. As demonstrated in Fig. 3, the surrogate model consists of two components: a Fourier Neural Operator (FNO) [31] that predicts 4D (3D space-time) CO₂ gas saturation distribution, followed by a convolutional neural network (CNN) that predicts the temporal evolution of trapped, free, and exited CO₂ given 4D gas saturation distribution.

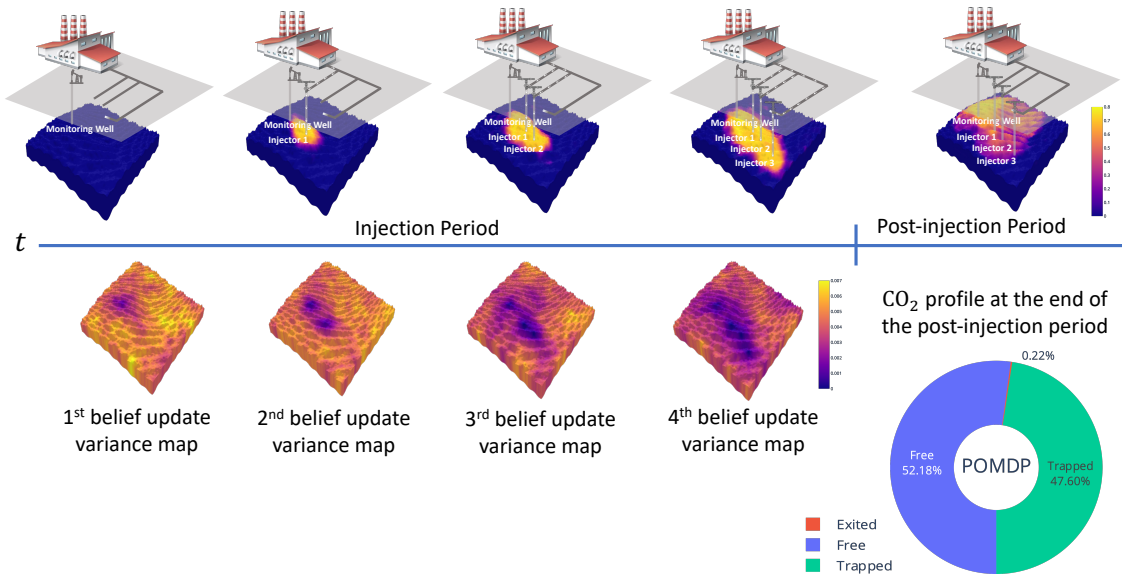
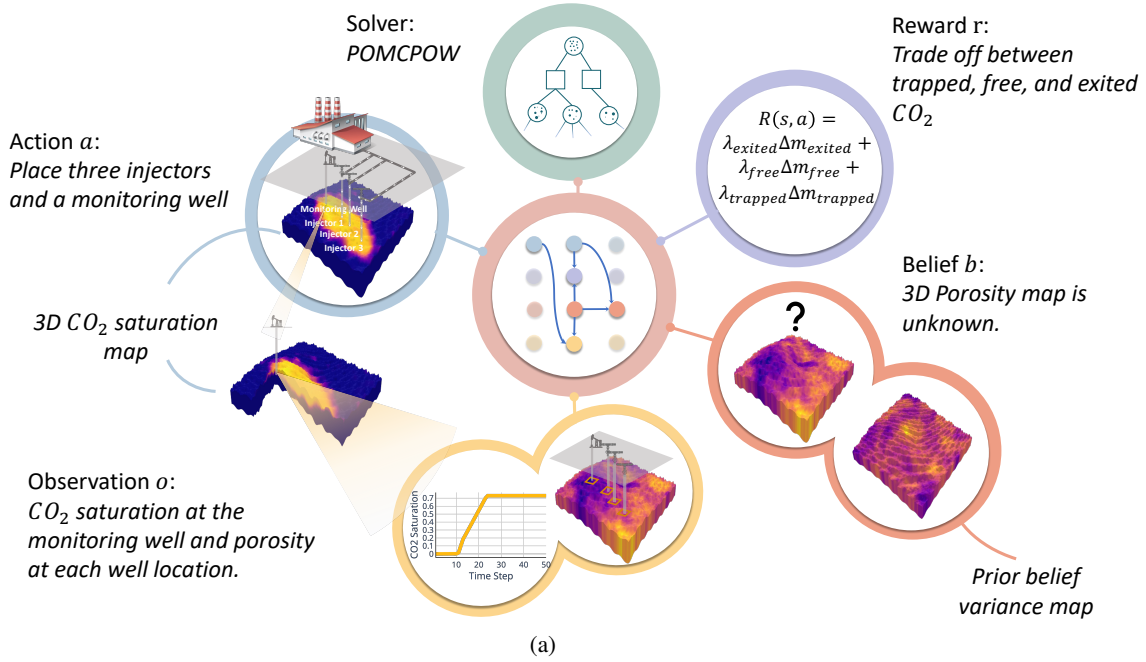
FNO is a type of neural operator [32] that uses the Fourier integral kernel operator to learn empirical relationships given input-output data pairs. FNO-typed architecture has shown superior accuracy and data efficiency for CO₂ storage compared to the previous convolutional neural network-based surrogate model problems [33, 34]. The input data to the injection period FNO model includes a combination of well locations, drilling strategy, porosity heterogeneity, rock compressibility, irreducible water/gas saturation, capillary entry pressure, water viscosity, as well as spatial and temporal encoding. Since all injection wells are shut down during the post-injection period, the well location and drilling strategy information are not needed by the post-injection FNO model. Instead, we provide the injection period gas saturation map to aid the prediction of the post-injection CO₂ migration.

We extend the original FNO architecture into 4D to predict the dynamic change of 3D gas saturation over 30 years of active injection and 500 years of post-injection monitoring. As shown in Fig. 3, the 3D spatial domain of the training data is an irregular geological formation. This leads to complex interactions between the flow behavior and gravity. The onset of and location of each injection well further increases the dimensionality of this problem. Nevertheless, the FNO architecture successfully learns this complex input-output 4D mapping with minimal overfitting. After obtaining the gas saturation prediction, we then use a CNN model to map the dynamic 3D gas saturation at each time step into time series predictions of CO₂ mass. The CNN architecture consists of three channels for trapped, free, and mobile CO₂ masses (see Extended Data Table 3–6 for details of the surrogate architecture and parameters). All training and test datasets utilized in this work were generated employing the MATLAB Reservoir Simulation Toolbox (MRST) [35], a versatile and widely recognized computational tool in the domain of reservoir simulations. Using the surrogate model, we obtain predictions with three orders of magnitude speed-up compared to traditional numerical simulators.

Results for the 3D case

In this work, we compare our proposed method with two baseline approaches. The first baseline, referred to as the random policy, involves selecting injectors randomly. The second baseline, called the expert policy, relies on experts utilizing their knowledge of the aquifer’s geological characteristics and the subsurface flow processes to determine injector locations. We evaluate the performance of the random, expert, and belief state planning policies.

Our approach makes decisions based on its belief at each time step. To illustrate the belief regarding the true porosity map, we present the variance maps of 100 sampled porosity maps from the belief after each decision step (posterior) in Fig. 2b. Darker colored areas signify lower variance, as the data acquired through drilling a well and observing CO₂ saturation over time via the monitoring well lead to greater certainty in the belief. Fig.4a summarizes the results due to



(b)

Figure 2: 3D saline aquifer carbon storage POMDP demonstration and its policy. (a) POMDP specification for individual components, emphasizing that the proposed belief state planning approach is a general methodology, without making specific claims about the superiority of a particular planner or parameter set. This allows operators and stakeholders to make trade-offs between various objectives. (b) The policy and overall performance of our approach in a single representative case, with 3D grids illustrating the aquifer structure.

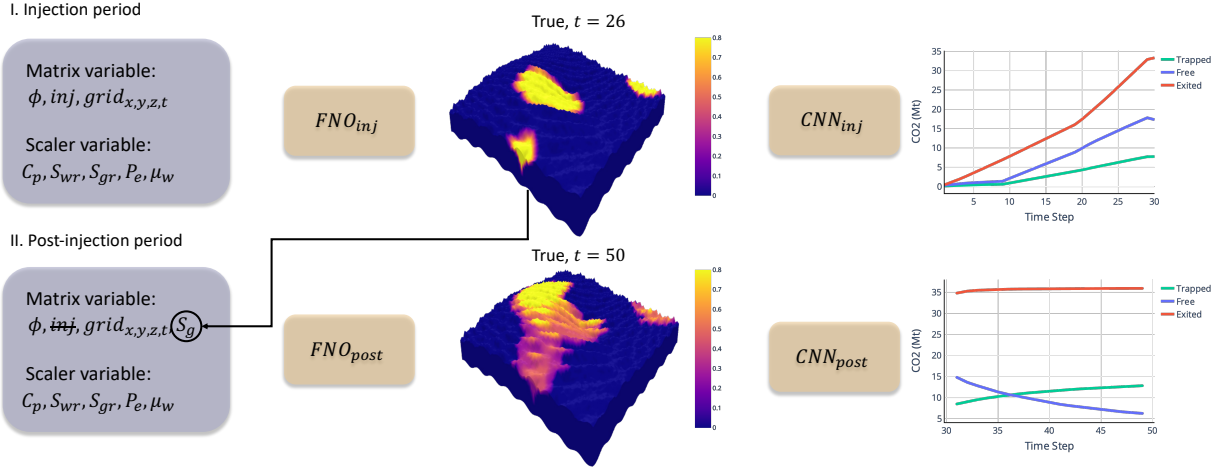


Figure 3: Surrogate model workflow for injection and post-injection period

different approaches on a single representative case. Our approach demonstrates superior performance, resulting in a 16.3% increase in trapped CO_2 and a 98.8% reduction in leaked CO_2 compared to the expert policy at the end of the post-injection period.

To comprehensively evaluate and compare the three approaches, we test their policies on ten cases with different 3D porosity maps as ground truths. Compared to the expert policies, the policies that result from our approach end up achieving 87% less exited CO_2 and 4% more trapped CO_2 (see Fig.4b). On the other hand, the random policies have a 2.9-fold increase in the quantity of exited CO_2 when compared to the expert policies. In addition, we use both mean and standard error of discounted return as metrics. As a result, our approach attains the highest expected discounted return across ten cases. A larger expected discounted return suggests a safer and more effective carbon capture policy. A smaller standard error of the discount return indicates a more robust performance around the expected discounted return. The results suggest our approach can provide robust performance compared to the other two baseline methods, ensuring safe and effective carbon storage operations.

Effects of Surrogate Model Fidelity Levels on Decision Quality

In this work, we use a trained surrogate model as a proxy for the complex decision environment, raising the question of how planning with different fidelity levels of the surrogate model might affect the performance of our proposed approach. To address this question, we trained surrogate models at two distinct fidelity levels. The high-fidelity model exhibits significantly smaller root mean squared errors (RMSE) in predicting CO_2 mass over time compared to its low-fidelity counterpart. For instance, the RMSE of trapped, free, and exited CO_2 mass predictions for the high-fidelity model are 1.1 MT, 1.8 MT, and 2.3 MT, respectively. Conversely, the corresponding RMSE values for the low-fidelity model are 1.8 MT, 2.8 MT, and 3.6 MT.

When comparing the density plots of errors between high and low fidelity surrogate model predictions of CO_2 mass and MRST outputs at the end of the post-injection period, we find that the error density plots of the high fidelity model are more closely centered around 0 and exhibit smaller variance than those of the low fidelity model (see Fig. 5a). We calculated the JS-divergences between the density curves, which are 0.0075, 0.0126, and 0.0057, respectively. The fidelity level of the surrogate models used in planning has a significant impact on decision quality. Fig. 5b shows that when planning with the high fidelity model, the density curve of the discounted return moves significantly to the right, indicating safer and more effective policies than planning with the low fidelity model. The JS-divergence between the two density plots on the discounted return due to high and low fidelity models is 42.2549, highlighting the significant impact that even small changes in the fidelity of the surrogate model can have on overall discounted returns.

In light of these results, the question naturally arises: "How accurate is accurate enough?" While it is clear that model accuracy plays a crucial role in the quality of the decision-making process, it is challenging to determine an exact threshold for sufficient accuracy. Practically, perfect accuracy is often unattainable, and operators must strike a balance

Mass profile at the end of post-injection period

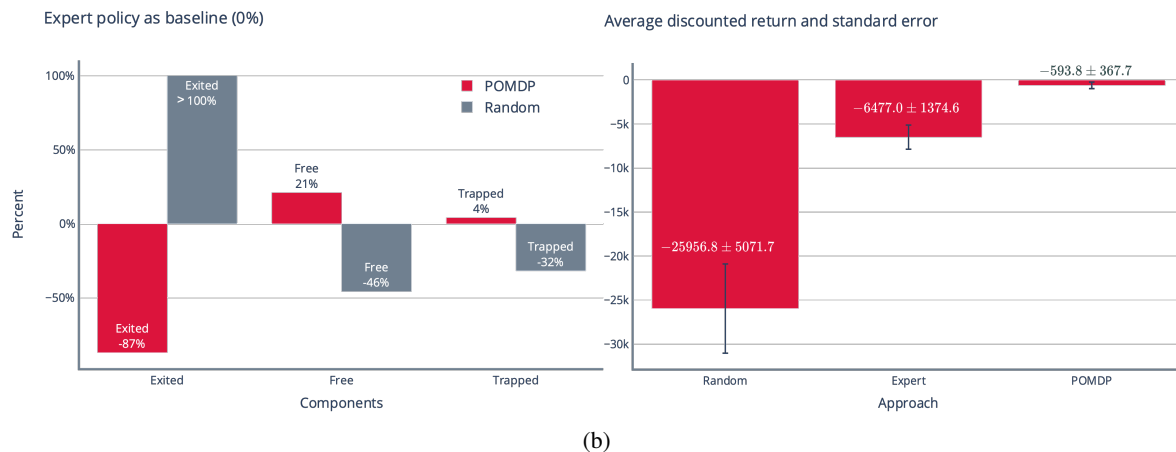
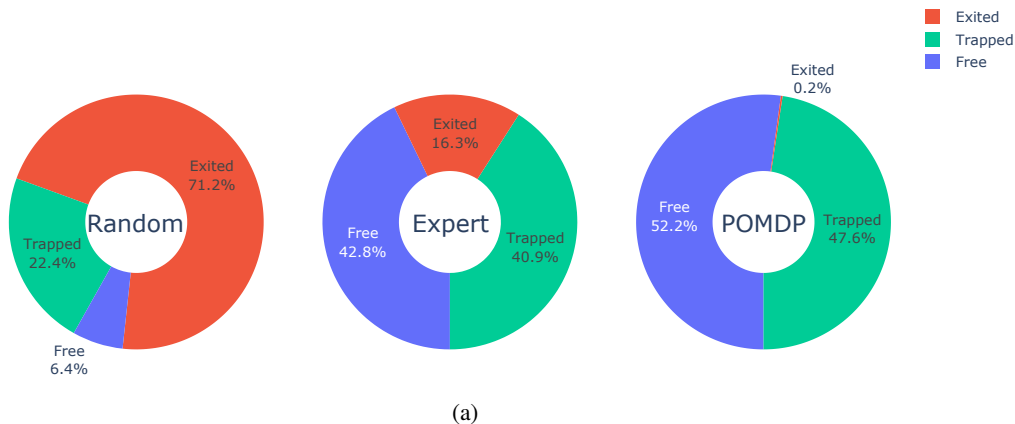


Figure 4: Performance comparison of three solution methods on the 3D example. (a) CO₂ mass profiles at the end of the post-injection period for a single representative case. (b) Aggregated performance metrics across ten cases.

between computational cost and model fidelity. The key takeaway from our analysis is that accuracy matters, but the surrogate model does not have to be perfect. We recommend that, as a best practice, any plan derived from a surrogate model should be validated using a higher fidelity model before implementation. This ensures that the most critical decisions are based on the most accurate information available, while still benefiting from the computational efficiency provided by surrogate models during the planning process.

Demonstrating the value of the monitoring well

As shown in Fig. 2, our approach needs to make sequential decisions on the locations of both the monitoring well and injectors. While it is common practice to include a monitoring well in the field to obtain subsurface information and monitor CO₂ saturation, our study, for the first time, quantifies the utility of the monitoring well in this context. Adding the monitoring well increases the complexity of making sequential decisions because of the alignment of the monitoring well with injectors to maximize information gain and better inform future actions. To evaluate the value and necessity of the monitoring well, we use the same POMDP formulation except without the monitoring well in the action space, resulting in a different observation space.

As shown in the first two rows of Table 1, planning with the monitoring well has a higher expected discounted reward and a lower standard error across ten cases. This suggests that the extra information from the monitoring well can enhance the decision quality.

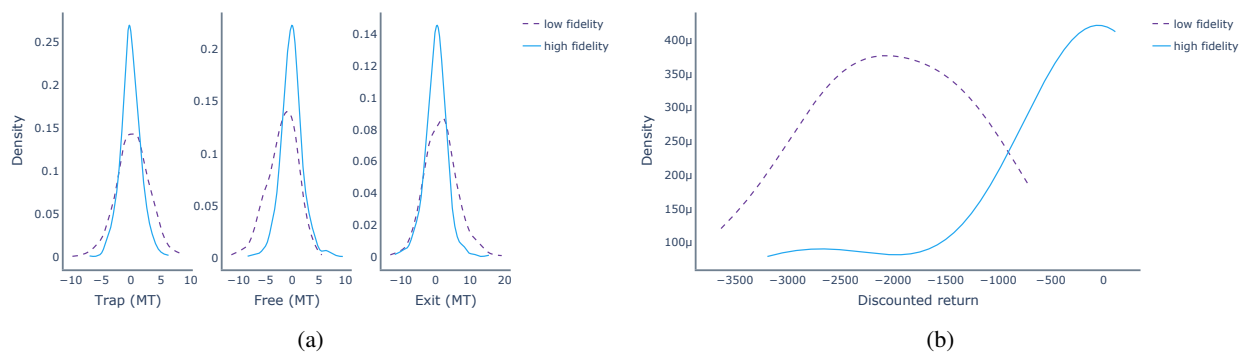


Figure 5: Comparative analysis of surrogate model fidelity. (a) Density plots illustrating the errors between the high and low fidelity surrogate predictions and MRST outputs. (b) Density plot on discounted return for high and low fidelity surrogate models across ten cases.

Table 1: Our proposed approach performance comparison under different observation strategies

Plan scenarios	Discounted return (mean \pm SE)	CO ₂ mass profile (MT) ^a		
		Trapped	Free	Exited
No monitoring well	-1262.9 \pm 485.3	30.5	26.9	1.6
Monitoring well	-593.8 \pm 367.7	30.9	27.2	0.9
4D seismic	- 475.8 \pm 157.8	30.4	27.8	0.8

^aThe values presented in the CO₂ mass profile represent the data collected at the conclusion of the post-injection phase.

Extending the point-wise observations to spatial observations

One of the key challenges in safe carbon storage operations is the lack of knowledge on CO₂ plume migration under complex geological regimes while planning. Geophysical monitoring (e.g., through seismic surveys) can provide predictions on CO₂ plume saturation and delineate its boundaries [36]. To demonstrate the possibility of adding seismic observations to the carbon storage POMDP, we replace placing the monitoring well with the ability to make seismic observations before drilling each injector in the action space of the 3D example. We mimic the seismic saturation observations by adding spatial filtering with Gaussian kernel [37] over the underlying true saturation map (see Extended Data Fig. 1 for an example). Among all the observation strategies outlined in Table 1, employing seismic observations in the planning process results in the safest policies and yields the highest discounted return and the lowest standard errors associated with it.

Discussion and conclusion

In this study, we address a sequential decision problem in carbon storage by employing belief state planning to ensure safe and effective operations. Our method significantly outperforms expert decisions in terms of expected discounted return and standard error across ten cases. For instance, in the representative 3D case, our proposed approach reduces the amount of leaked CO₂ by over 87% when compared to the expert policy. Furthermore, we find that incorporating information from monitoring wells and seismic observations allows our approach to achieving safer and more effective policies.

To make planning under a multi-phase flow environment feasible, we train an FNO neural network as a surrogate flow simulator. We investigate the impact of different fidelity levels of the surrogate model on the decision quality of our proposed approach. Our results indicate that planning with a high-fidelity model leads to substantially safer and more effective decisions for carbon storage operations. Large-scale simulations serve as an effective means of evaluating our methodology, as physical experiments would not only take years to complete but also fail to adequately assess the robustness of the decision strategies. Moreover, it would be challenging to fairly compare various methodologies across a broad range of scenarios using physical experiments alone.

As the development of carbon storage projects gains momentum globally, ensuring the safe operation of these initiatives is of paramount importance. Our research highlights the potential necessity of our proposed approach in ensuring the long-term safety of carbon storage projects.

Data availability

The data used for this work is made available in the repository <https://github.com/yizhengw/OptimizingCarbonStorage>.

Code availability

The code used to produce the results for this work is made available in the repository <https://github.com/yizhengw/OptimizingCarbonStorage>.

References

- [1] *United Nations Environment Programme (2022). Emissions Gap Report 2022: The closing window — climate crisis calls for rapid transformation of societies. Nairobi. See <https://www.unep.org/emissions-gap-report-2022/> (accessed 10 December 2022).*
- [2] *IPCC. 2018 Global Warming of 1.5°C. An IPCC special report on the impacts of global warming of 1.5°C above pre-industrial levels and related global greenhouse gas emission pathways, in the context of strengthening the global response to the threat of climate change, sustainable development, and efforts to eradicate poverty. See <https://www.ipcc.ch/sr15/> (accessed 10 December 2022).*
- [3] Christian LE Franzke. Nonlinear climate change. *Nature Climate Change*, 4(6):423–424, 2014.
- [4] Robert WR Parker, Julia L Blanchard, Caleb Gardner, Bridget S Green, Klaas Hartmann, Peter H Tyedmers, and Reg A Watson. Fuel use and greenhouse gas emissions of world fisheries. *Nature Climate Change*, 8(4):333–337, 2018.
- [5] Kevin E Trenberth, Aiguo Dai, Gerard Van Der Schrier, Philip D Jones, Jonathan Barichivich, Keith R Briffa, and Justin Sheffield. Global warming and changes in drought. *Nature Climate Change*, 4(1):17–22, 2014.
- [6] Jon Norberg, Mark C Urban, Mark Vellend, Christopher A Klausmeier, and Nicolas Loeuille. Eco-evolutionary responses of biodiversity to climate change. *Nature Climate Change*, 2(10):747–751, 2012.
- [7] David EHJ Gernaat, Harmen Sytze de Boer, Vassilis Daioglou, Seleshi G Yalew, Christoph Müller, and Detlef P van Vuuren. Climate change impacts on renewable energy supply. *Nature Climate Change*, 11(2):119–125, 2021.
- [8] Shahrouz Abolhosseini, Almas Heshmati, and Jorn Altmann. A review of renewable energy supply and energy efficiency technologies. 2014.
- [9] Diana Silva Siqueira, Josué de Almeida Meystre, Maicon Queiroz Hilário, Danilo Henrique Donato Rocha, Genésio José Menon, and Rogério José da Silva. Current perspectives on nuclear energy as a global climate change mitigation option. *Mitigation and Adaptation Strategies for Global Change*, 24(5):749–777, 2019.
- [10] Ronald Wennersten, Qie Sun, and Hailong Li. The future potential for carbon capture and storage in climate change mitigation—an overview from perspectives of technology, economy and risk. *Journal of Cleaner Production*, 103:724–736, 2015.
- [11] Milenka Mitrović and Alexandra Malone. Carbon capture and storage (CCS) demonstration projects in canada. *Energy Procedia*, 4:5685–5691, 2011.
- [12] Bert Metz, Ogunlade Davidson, HC De Coninck, Manuela Loos, and Leo Meyer. IPCC special report on carbon dioxide capture and storage. 2005.
- [13] *International Energy Agency. 2020 CCUS in the transition to net-zero emissions. See <https://www.iea.org/reports/ccus-in-clean-energy-transitions/ccus-in-the-transition-to-net-zero-emissions> (accessed 10 December 2022).*
- [14] Glen P Peters, Robbie M Andrew, Tom Boden, Josep G Canadell, Philippe Ciais, Corinne Le Quéré, Gregg Marland, Michael R Raupach, and Charlie Wilson. The challenge to keep global warming below 2 c. *Nature Climate Change*, 3(1):4–6, 2013.
- [15] Mouadh Addassi, Abdirizak Omar, Hussein Hoteit, Abdulkader M Afifi, Serguey Arkadaskiy, Zeyad T Ahmed, Noushad Kunnummal, Sigurdur R Gislason, and Eric H Oelkers. Assessing the potential of solubility trapping in unconfined aquifers for subsurface carbon storage. *Scientific Reports*, 12(1):1–15, 2022.

- [16] Zaixing Huang, Christine Sednek, Michael A Urynowicz, Hongguang Guo, Qiurong Wang, Paul Fallgren, Song Jin, Yan Jin, Uche Igwe, and Shengpin Li. Low carbon renewable natural gas production from coalbeds and implications for carbon capture and storage. *Nature Communications*, 8(1):1–11, 2017.
- [17] Karsten Michael, Alexandra Golab, Valeriya Shulakova, Jonathan Ennis-King, Guy Allinson, Sandeep Sharma, and Toby Aiken. Geological storage of CO₂ in saline aquifers—a review of the experience from existing storage operations. *International Journal of Greenhouse Gas Control*, 4(4):659–667, 2010.
- [18] IEA (2022), *CO₂ storage resources and their development*, IEA, Paris. <https://www.iea.org/reports/co2-storage-resources-and-their-development> (accessed 12 December 2022).
- [19] Céline Scheidt, Lewis Li, and Jef Caers. Quantifying uncertainty in subsurface systems. *John Wiley & Sons*, 236, 2018.
- [20] Daniel M Tartakovsky. Assessment and management of risk in subsurface hydrology: A review and perspective. *Advances in Water Resources*, 51:247–260, 2013.
- [21] MA Celia, S Bachu, JM Nordbotten, and KW Bandilla. Status of CO₂ storage in deep saline aquifers with emphasis on modeling approaches and practical simulations. *Water Resources Research*, 51(9):6846–6892, 2015.
- [22] Sandra Ó Snæbjörnsdóttir, Bergur Sigfússon, Chiara Marieni, David Goldberg, Sigurður R Gislason, and Eric H Oelkers. Carbon dioxide storage through mineral carbonation. *Nature Reviews Earth & Environment*, 1(2):90–102, 2020.
- [23] Mykel J Kochenderfer, Tim A Wheeler, and Kyle H Wray. Algorithms for decision making. *MIT Press*, 2022.
- [24] David Silver, Julian Schrittwieser, Karen Simonyan, Ioannis Antonoglou, Aja Huang, Arthur Guez, Thomas Hubert, Lucas Baker, Matthew Lai, Adrian Bolton, et al. Mastering the game of go without human knowledge. *Nature*, 550(7676):354–359, 2017.
- [25] Xuanchen Xiang and Simon Foo. Recent advances in deep reinforcement learning applications for solving partially observable Markov decision processes (POMDP) problems: Part 1—fundamentals and applications in games, robotics and natural language processing. *Machine Learning and Knowledge Extraction*, 3(3):554–581, 2021.
- [26] Wenqian Zhang and Haiyan Wang. Diagnostic policies optimization for chronic diseases based on POMDP model. In *Healthcare*, volume 10, page 283. MDPI, 2022.
- [27] Constantin Hubmann, Nils Quetschlich, Jens Schulz, Julian Bernhard, Daniel Althoff, and Christoph Stiller. A pomdp maneuver planner for occlusions in urban scenarios. In *2019 IEEE Intelligent Vehicles Symposium (IV)*, pages 2172–2179. IEEE, 2019.
- [28] Yizheng Wang, Markus Zechner, John Michael Mern, Mykel J Kochenderfer, and Jef Karel Caers. A sequential decision-making framework with uncertainty quantification for groundwater management. *Advances in Water Resources*, 166:104266, 2022.
- [29] Thomas M Daley, Ray D Solbau, Jonathan B Ajo-Franklin, and Sally M Benson. Continuous active-source seismic monitoring of CO₂ injection in a brine aquifer. *Geophysics*, 72(5):A57–A61, 2007.
- [30] James P Verdon, J-Michael Kendall, Don J White, Doug A Angus, Quentin J Fisher, and Ted Urbancic. Passive seismic monitoring of carbon dioxide storage at weyburn. *The Leading Edge*, 29(2):200–206, 2010.
- [31] Zongyi Li, Nikola Kovachki, Kamyar Azizzadenesheli, Burigede Liu, Kaushik Bhattacharya, Andrew Stuart, and Anima Anandkumar. Fourier neural operator for parametric partial differential equations. *arXiv preprint arXiv:2010.08895*, 2020.
- [32] Zongyi Li, Nikola Kovachki, Kamyar Azizzadenesheli, Burigede Liu, Andrew Stuart, Kaushik Bhattacharya, and Anima Anandkumar. Multipole graph neural operator for parametric partial differential equations. *Advances in Neural Information Processing Systems*, 33:6755–6766, 2020.
- [33] Gege Wen, Zongyi Li, Kamyar Azizzadenesheli, Anima Anandkumar, and Sally M Benson. U-fno — an enhanced fourier neural operator-based deep-learning model for multiphase flow. *Advances in Water Resources*, 163:104180, 2022.
- [34] Gege Wen, Zongyi Li, Qirui Long, Kamyar Azizzadenesheli, Anima Anandkumar, and Sally M Benson. Accelerating carbon capture and storage modeling using fourier neural operators. *arXiv preprint arXiv:2210.17051*, 2022.
- [35] Knut-Andreas Lie. An introduction to reservoir simulation using matlab/gnu octave: User guide for the matlab reservoir simulation toolbox (mrst). 2019.

- [36] Manzar Fawad and Nazmul Haque Mondol. Monitoring geological storage of CO₂: A new approach. *Scientific Reports*, 11(1):1–9, 2021.
- [37] Chanda Bhabatosh et al. Digital image processing and analysis. *PHI Learning Pvt. Ltd.*, 1977.

Methods

POMDPs

A POMDP is a model for sequential decision making under uncertainty. A POMDP is defined as a tuple $(\mathcal{S}, \mathcal{A}, \mathcal{O}, O, T, R, \gamma)$, where \mathcal{S} is the set of states, \mathcal{A} is the set of actions, \mathcal{O} is the set of observations, O is the observation function, T is the state transition function, R is the reward function, and γ is the discount factor. At each step, an agent in state $s \in \mathcal{S}$ takes action $a \in \mathcal{A}$, transitions to the next state $s' \in \mathcal{S}$ with probability $T(s' | s, a)$ and receives both an observation $o \in \mathcal{O}$ with probability $O(o | s', a)$ and a reward $r = R(s, a, s')$. In a POMDP, the underlying state of the environment is not fully known. Instead, the agent maintains a distribution over states called a belief $b(s)$. The agent infers its belief from the history of observations and actions according to Bayes’s rule, $b'(s') = p(s' | b, a, o) \propto O(o | s', a) \sum_{s \in \mathcal{S}} T(s' | s, a)b(s)$.

A policy is a function that maps beliefs to actions. The goal is to find the optimal policy π^* that maximizes the expected sum of discounted reward, $\sum_{t=1}^n \gamma^{t-1} r_t$. For the infinite horizon sequential problem where $n \rightarrow \infty$, the discounted factor $\gamma \in [0, 1)$ is introduced to bound the total discounted reward.

In general, there are two approaches to generating a policy for POMDPs: offline or online during action execution. Offline solvers perform most of the computation prior to interacting with the environment while online solvers perform computation between state transitions.

3D saline aquifer example

The 3D aquifer grids have an extension of eighty grid blocks in the x- and the y-direction (lateral extension) and eight blocks in the z-direction (depth). There are three injectors and one monitoring well. The monitoring well needs to be placed before any injectors. The three injectors are placed in a time sequence at the 1st, 11th, and 21st years. The injection period and post-injection period, respectively, are 30 and 500 years resulting in a total of 530 years of simulation time. We assume permeability K follows a deterministic function of porosity ϕ , with $K = \frac{10^{-10} \phi^3}{58.32(1-\phi)^2}$. Therefore, our approach only needs to keep track of the porosity map in its state space and observes porosity values at each well location (see Extended Data Table 1-2 for specific values of geological, engineering, POMDP, and planner parameters).

Surrogate model training details

For both the injection and post-injection surrogate models, we train the saturation and mass separately. We trained the gas situation FNO models using 300 training samples and 100 test samples for around 300 epochs. Each epoch takes approximately 3 mins. For the CO₂ mass CNN models, we trained with 600 training samples and 100 test samples for around 300 epochs. Each epoch takes approximately 11 s. CO₂ mass requires more training samples because it is more prone to overfitting. The relative squared-error loss is used for both scenarios to ensure effective gradient propagation. After training, the average gas saturation error given unseen inputs is 0.013 during the injection period and 0.016 during the post-injection period. The average mass error (defined as the mean absolute error divided by the mass norm) is 0.012 during the injection period and 0.015 during the post-injection period. To obtain surrogate models with two distinct fidelity levels, we utilize 12,000 training data for the high-fidelity model and 1,700 training data for the low-fidelity model.

Partially Observable Monte Carlo Planning with Observation Widening

Due to the relatively long time scales expected in CCS, we use an online solver called Partially Observable Monte Carlo Planning with Observation Widening (POMCPOW). POMCPOW is a tree search algorithm used for online decision-making, which can effectively handle continuous state, action, and observation spaces [38]. Prior to POMCPOW, state-of-the-art online planners such as POMCP and DESPOT struggled to solve POMDPs with continuous observation spaces [39, 40]. Their planning trees suffer from belief collapse beyond the root node and end up generating suboptimal policies. POMCPOW, on the other hand, creates weighted particle-based search trees, resulting in richer belief representations at each node, allowing the search trees to grow deeper. Richer beliefs also make generated policies

contain information-gathering actions and thus yield better strategies for the problems where information-gathering is needed.

Ensemble Smoother with Multiple Data Assimilation

Ensemble Smoother with Multiple Data Assimilation (ES-MDA) is a commonly used ensemble-based inference method for estimating state uncertainties [41]. Unlike Bayesian inversion using Markov chain Monte Carlo (MCMC) methods to obtain posterior distributions, ensemble-based methods can significantly reduce the computational cost of belief updates. Among the ensemble-based methods, the ensemble Kalman filter (EnKF) is one of the most popular approaches [42]. However, the recurrent simulation restarts required in the EnKF sequential data simulation process make this method impractical for problems that involve expensive forward simulations. On the other hand, in ensemble smoother (ES), all data are assimilated simultaneously in a single update [43]. Therefore, there is no need for simulation restarts, which makes it more attractive for practical applications. However, because ES computes a single update, it may not yield a good result that matches the data. In order to fix this problem, ES-MDA introduces an inflation factor (α) in front of the data-error covariance matrix C_D . This factor helps the algorithm to correctly sample from the posterior distribution [44].

Belief update

The porosity map is partially observable. However, the belief over the porosity map can be informed by both direct measurements of aquifer porosity at each well location and CO₂ saturation history. Because observations are obtained from two different sources, the belief update is formulated as follows:

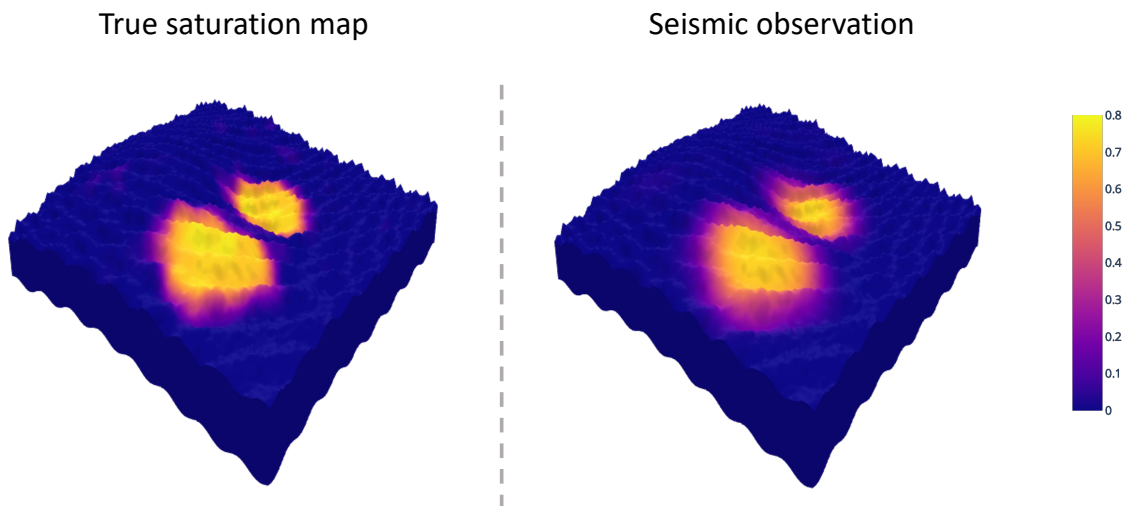
$$p(\phi \mid d_1, \mathbf{d}_2) = \sum_{\phi_{\text{cond}}} p(\phi \mid \phi_{\text{cond}}, \mathbf{d}_2) p(\phi_{\text{cond}} \mid d_1) \quad (1)$$

where ϕ stands for the porosity maps, d_1 is the observed porosity value, and \mathbf{d}_2 is the observed CO₂ saturation history at the monitoring well. The term ϕ_{cond} represents the conditional porosity maps with only d_1 using conditional Gaussian simulation [45]. Therefore, we can assume ϕ is conditional independent with d_1 , statistically represented as $p(\phi \mid d_1, \mathbf{d}_2, \phi_{\text{cond}}) = p(\phi \mid \mathbf{d}_2, \phi_{\text{cond}})$.

To reduce the computational cost of solving the inversion problem with high dimensional data, we deploy ES-MDA to sample from the posterior of ϕ given both \mathbf{d}_2 and ϕ_{cond} .

References

- [38] Zachary N Sunberg and Mykel J Kochenderfer. Online algorithms for POMDPs with continuous state, action, and observation spaces. In *International Conference on Automated Planning and Scheduling*, 2018.
- [39] Adhiraj Somani, Nan Ye, David Hsu, and Wee Sun Lee. Despot: Online POMDP planning with regularization. *Advances in Neural Information Processing Systems*, 26, 2013.
- [40] David Silver and Joel Veness. Monte-Carlo planning in large POMDPs. *Advances in Neural Information Processing Systems*, 23, 2010.
- [41] Alexandre A Emerick and Albert C Reynolds. Ensemble smoother with multiple data assimilation. *Computers & Geosciences*, 55:3–15, 2013.
- [42] Geir Evensen. The ensemble kalman filter: Theoretical formulation and practical implementation. *Ocean Dynamics*, 53(4):343–367, 2003.
- [43] J-A Skjervheim, Geir Evensen, Joakim Hove, Jon G Vabø, et al. An ensemble smoother for assisted history matching. In *SPE Reservoir Simulation Symposium*. OnePetro, 2011.
- [44] Alexandre A Emerick. Analysis of the performance of ensemble-based assimilation of production and seismic data. *Journal of Petroleum Science and Engineering*, 139:219–239, 2016.
- [45] Masaru Hoshiya. Kriging and conditional simulation of Gaussian field. *Journal of Engineering Mechanics*, 121(2):181–186, 1995.



Extended Data Fig. 1: Seismic observation example for a given 3D saturation map

Extended Data Table 1: Geological and engineering parameters for the 3D aquifer

Variable Description	Value
Porosity map mean	0.2
Porosity map variogram sill	0.001
Porosity map variogram range	20.0
Porosity map variogram nugget	0.0001
Rock compressibility	4.35×10^{-5}
Irreducible water saturation	0.27
Irreducible gas saturation	0.20
Capillary entry pressure	5.0
Water viscosity	8×10^{-4}

Extended Data Table 2: POMDP and POMCPOW hyperparameters

Variable Description	Value
Discount Factor (γ)	0.99
λ_{exited}	-1000.0
λ_{free}	-1.0
λ_{trapped}	10.0
Gaussian filtering kernel σ	3.0
Distribution of observation noise	$\mathcal{N}(0, 0.1 \times \phi_{\text{obs}})$
Exploration Coefficient for UCB	20.0
Observation widening exponent (α_{obs})	0.7
Observation widening coefficient (k_{obs})	5.0
Action widening exponent (α_{act})	0.7
Action widening coefficient (k_{act})	2.0
Number of tree queries (N_{query})	100

Extended Data Table 3: Model parameters for gas saturation during the injection period. The Padding denotes a padding operator that accommodates the non-periodic boundaries; Linear denotes the linear transformation to lift the input to the high dimensional space and the projection back to the original space; Fourier4d denotes the 4D Fourier operator; Conv1d denotes the bias term; Add operation adds the outputs together; GELU denotes a Gaussian Error Linear Units layer.

Layer	Operation	Output Shape
Input	-	(30, 80, 80, 8, 11)
Padding	Padding (4)	(38, 88, 88, 16, 11)
Lifting	Linear	(38, 88, 88, 16, 28)
Fourier 1	Fourier4d/Conv1d/Add/GELU	(38, 88, 88, 16, 28)
Fourier 2	Fourier4d/Conv1d/Add/GELU	(38, 88, 88, 16, 28)
Fourier 3	Fourier4d/Conv1d/Add/GELU	(38, 88, 88, 16, 28)
Fourier 4	Fourier4d/Conv1d/Add	(30, 80, 80, 8, 28)
De-padding	Depadding (4)	(30, 80, 80, 8, 28)
Projection 1	Linear	(30, 80, 80, 8, 64)
Projection 2	Linear	(30, 80, 80, 8, 1)

Extended Data Table 4: Model parameters for CO₂ mass during the injection period. After the flattening layer, the model splits into three channels where each channel contains an FC1 and FC2.

Layer	Operation	Output Shape
Input	-	(30, 80, 80, 8)
Conv1	Conv3D/BN/ReLU	(30, 40, 40, 4)
Conv2	Conv3D/BN/ReLU	(30, 20, 20, 2)
Flatten	-	(1, 24000)
FC1	FC/BN/ReLU	(1, 100)
FC2	FC/BN/ReLU	(1, 30)

Extended Data Table 5: Model parameters for gas saturation during post-injection period. The Padding denotes a padding operator that accommodates the non-periodic boundaries; Linear denotes the linear transformation to lift the input to the high dimensional space and the projection back to the original space; Fourier4d denotes the 4D Fourier operator; Conv1d denotes the bias term; Add operation adds the outputs together; GELU denotes a Gaussian Error Linear Units layer.

Layer	Operation	Output Shape
Input	-	(20, 80, 80, 8, 11)
Padding	Padding (4)	(28, 88, 88, 16, 11)
Lifting	Linear	(28, 88, 88, 16, 28)
Fourier 1	Fourier4d/Conv1d/Add/GELU	(28, 88, 88, 16, 28)
Fourier 2	Fourier4d/Conv1d/Add/GELU	(28, 88, 88, 16, 28)
Fourier 3	Fourier4d/Conv1d/Add/GELU	(28, 88, 88, 16, 28)
Fourier 4	Fourier4d/Conv1d/Add	(20, 80, 80, 8, 28)
De-padding	Depadding (4)	(20, 80, 80, 8, 28)
Projection 1	Linear	(20, 80, 80, 8, 64)
Projection 2	Linear	(20, 80, 80, 8, 1)

Extended Data Table 6: Model parameters for CO₂ mass during the post-injection period. After the flattening layer, the model splits into three channels where each channel contains an FC1 and FC2.

Layer	Operation	Output Shape
Input	-	(20, 80, 80, 8)
Conv1	Conv3D/BN/ReLU	(20, 40, 40, 4)
Conv2	Conv3D/BN/ReLU	(20, 20, 20, 2)
Flatten	-	(1, 16000)
FC1	FC/BN/ReLU	(1, 100)
FC2	FC/BN/ReLU	(1, 20)